

# Radiative falloff in Einstein-Straus spacetime

William G. Laarakkers and Eric Poisson

*Department of Physics, University of Guelph, Guelph, Ontario, Canada N1G 2W1*

(Submitted to Physical Review D, May 3, 2001)

The Einstein-Straus spacetime describes a nonrotating black hole immersed in a matter-dominated cosmology. It is constructed by scooping out a spherical ball of the dust and replacing it with a vacuum region containing a black hole of the same mass. The metric is smooth at the boundary, which is comoving with the rest of the universe. We study the evolution of a massless scalar field in the Einstein-Straus spacetime, with a special emphasis on its late-time behavior. This is done by numerically integrating the scalar wave equation in a double-null coordinate system that covers both portions (vacuum and dust) of the spacetime. We show that the field's evolution is governed mostly by the strong concentration of curvature near the black hole, and the discontinuity in the dust's mass density at the boundary; these give rise to a rather complex behavior at late times. Contrary to what it would do in an asymptotically-flat spacetime, the field does not decay in time according to an inverse power-law.

## I. INTRODUCTION

The dynamics of radiative fields in spacetimes containing a black hole has been the subject of many investigations, some analytical [1–9], some numerical [10–15], some restricted to nonrotating black holes [1–6,10,11], and some devoted to rotating black holes [7–9,12–15]. Most of these studies were concerned with black holes immersed in an asymptotically-flat spacetime. In such cases, radiative dynamics always proceeds in the same three stages. First, an outburst of radiation is emitted, as determined by the initial conditions imposed on the radiative field; most of this radiation proceeds directly to infinity, with only mild distortions produced by the spacetime curvature. Second, the radiation begins to oscillate, with frequencies and damping times determined by the properties of the black hole; these oscillations are produced by the part of the initial outburst that does not go directly to infinity, but interacts with the high concentration of curvature near the black hole. Third, the oscillations stop, and the field decays monotonically, as an inverse power-law in time; the power is determined by the radiation's multipole order  $l$ .

A number of authors have studied radiative dynamics in black-hole spacetimes that are not asymptotically flat. Brady, Chambers, Krivan, and Laguna [16] considered the evolution of a massless scalar field in Reissner-Nordstöm-de Sitter spacetime, which describes a charged black hole immersed in an exponentially expanding universe. They found that while the first two stages of radiative dynamics are not affected by the different conditions at infinity, the third one is: at late times the field decays exponentially, not as an inverse power-law. This new type of behavior was explored more thoroughly by Brady, Chambers, Laarakkers, and Poisson [17], who showed that the decay constant can be complex if the scalar field is nonminimally coupled to the curvature: the

field oscillates as it decays exponentially. While these authors were concerned with black-hole spacetimes with a positive cosmological constant, other authors have examined radiative dynamics in the presence of a negative cosmological constant [18–21]; they also find an exponential decay.

The literature reviewed in the preceding paragraph indicates that inverse power-law decay is a property of asymptotically-flat spacetimes, and that different behaviors should be expected in black-hole spacetimes that have different asymptotic properties. This conclusion has been reinforced by a number of analytical studies [3,6]. Our goal with this paper is to contribute further to the exploration of radiative dynamics in black-hole spacetimes that are not asymptotically flat. Here we consider the evolution of a massless scalar field in the spacetime of a nonrotating black hole immersed in a matter-dominated cosmology. We investigate the effect of the cosmological asymptotics on the late-time behavior of the radiation.

To construct the spacetime we start with a homogeneous, isotropic, dust-filled universe and we remove from it a spherical ball of the dust, which we replace by a vacuum region containing a black hole of the same mass. The boundary between the vacuum and the dust is comoving with the rest of the universe. Its dynamics is determined by the curvature of the spatial sections: it expands forever for zero and negative curvature, and it eventually recontracts for positive curvature. This construction was first carried out by Einstein and Straus in 1945 [22]. We reproduce it in Sec. II, where we also introduce a single coordinate system to cover both regions (vacuum and dust) of the spacetime. In Sec. III we write down the second-order partial differential equation that governs the evolution of a massless scalar field  $\Phi$  in this spacetime. After separation of the variables, the field equation reduces to a two-dimensional wave equa-

tion with an effective potential. This wave equation is numerically integrated in Sec. IV, where we present our main results.

Radiative dynamics in the Einstein-Straus spacetime is governed mostly by the strong concentration of curvature near the black hole, and the discontinuity in the dust's mass density at the boundary. These features are encoded in the effective potential, which possesses a fairly well localized barrier near the black hole's event horizon, and a jump discontinuity at the boundary. A wave propagating in the presence of this potential will be partially transmitted and reflected each time it encounters the barrier or the jump. These processes give rise to a rather complex late-time behavior for the radiation — the field does not decay according to an inverse power-law. We describe this behavior in detail in Sec. IV. In Sec. V we seek insight into the multiple transmissions and reflections that take place between the event horizon and the boundary by working through a simple toy model.

We believe that radiative dynamics in the Einstein-Straus spacetime provides an excellent illustration of the general fact that inverse power-law falloff can occur only in asymptotically-flat spacetimes. This article contributes to an ongoing effort to explore the rich spectrum of behaviors that results when asymptotic flatness is replaced by different asymptotic conditions.

Throughout the paper we work in relativistic units, in which  $c = G = 1$ .

## II. EINSTEIN-STRAUS SPACETIME

The Einstein-Straus spacetime [22] represents a non-rotating black hole immersed in a cosmological universe containing a pressureless fluid (which we shall call dust). It is constructed by scooping out a spherical ball of the dust and replacing it with a vacuum region containing a black hole of the same mass. The mathematical description of the spacetime involves two metrics joined at a common boundary  $\Sigma$ . The metric inside the boundary is given by the Schwarzschild solution, the metric outside is one of the Friedmann-Lemaître-Robertson-Walker (FLRW) metrics, and  $\Sigma$  is a three-dimensional hypersurface generated by timelike geodesics of both spacetimes.

The boundary is comoving with the universe; it expands forever if the universe has spatial sections that are flat ( $k = 0$ ) or have negative curvature ( $k = -1$ ), or it expands to a maximum radius and recontracts if the spatial sections have positive curvature ( $k = 1$ ). As seen from the Schwarzschild side, the boundary is either gravitationally bound to the black hole (if  $k = 1$ ), or it is unbound or just marginally bound (if  $k = -1$  or  $k = 0$ , respectively). The spacetime is depicted, by means of a conformal diagram, in Fig. 1; in this figure the boundary is assumed to expand forever.

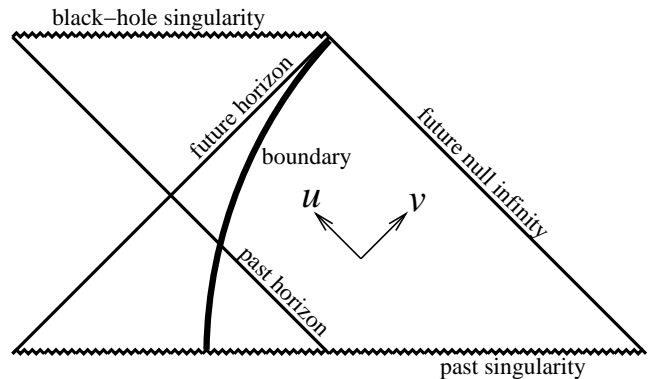


FIG. 1. The Einstein-Straus spacetime, as represented by a conformal diagram. The Schwarzschild region is on the left-hand side of the boundary, and the FLRW region is on the right-hand side. It is assumed that the cosmological region possesses flat spatial sections, so that the boundary expands forever. The portion of the spacetime bounded by the past singularity, the future horizon, and future null infinity can be covered by the  $u$  and  $v$  coordinates introduced in the text. In the diagram,  $u$  increases at 45 degrees toward the left, while  $v$  increases at 45 degrees toward the right. The future horizon is located at  $u = \infty$ , future null infinity at  $v = \infty$ , the boundary at  $v - u = 2\chi_0$ , and the past horizon at  $v = 3\chi_0$ .

### A. Joining the metrics at the boundary

The metric inside  $\Sigma$  is expressed in the usual Schwarzschild coordinates as

$$ds_{\text{in}}^2 = -f dt^2 + f^{-1} dr^2 + r^2 d\Omega^2, \quad (2.1)$$

where  $f = 1 - 2M/r$  and  $d\Omega^2 = d\theta^2 + \sin^2\theta d\phi^2$ ;  $M$  is the gravitational mass of the black hole. The metric of Eq. (2.1) is valid for  $r < r_\Sigma(\tau)$ , where  $r_\Sigma$  is the changing radius of the timelike hypersurface  $\Sigma$ ;  $\tau$  is proper time for observers comoving with the boundary. Because the hypersurface is generated by timelike geodesics, its equations of motion are  $\dot{t} = \tilde{E}/f$  and  $\dot{r}^2 + f = \tilde{E}^2$ . Here, an overdot indicates differentiation with respect to  $\tau$ , and  $\tilde{E}$  is the usual conserved-energy parameter.

For bound motion ( $\tilde{E} < 1$ ), the solution to the equations of motion can be expressed in the parametric form

$$r_\Sigma(\eta) = \frac{1}{2} r_{\text{max}}(1 - \cos \eta), \quad (2.2)$$

$$\tau(\eta) = \frac{1}{2} r_{\text{max}} \sqrt{r_{\text{max}}/2M} (\eta - \sin \eta),$$

in terms of a conformal-time parameter  $\eta$ ; the constant  $r_{\text{max}} \equiv 2M/(1 - \tilde{E}^2)$  represents the boundary's maximum radius. For unbound motion ( $\tilde{E} > 1$ ), the solution is

$$r_{\Sigma}(\eta) = \frac{1}{2} r_0 (\cosh \eta - 1), \quad (2.3)$$

$$\tau(\eta) = \frac{1}{2} r_0 \sqrt{r_0/2M} (\sinh \eta - \eta),$$

where  $r_0 \equiv 2M/(\tilde{E}^2 - 1)$ . Finally, for marginally bound motion ( $\tilde{E} = 1$ ) we have

$$r_{\Sigma}(\tau) = \frac{9M}{2} \left( \frac{2\tau}{9M} \right)^{2/3}. \quad (2.4)$$

The metric outside  $\Sigma$  is expressed as

$$ds_{\text{out}}^2 = a^2(\eta) [-d\eta^2 + d\chi^2 + s^2(\chi) d\Omega^2], \quad (2.5)$$

where  $\eta$  is conformal time,  $\chi$  a radial coordinate,  $a(\eta)$  the cosmological scale factor, and  $s(\chi)$  a function that determines the geometry of the spatial sections:

$$s(\chi) = \begin{cases} \sin \chi & k = 1 \\ \chi & k = 0 \\ \sinh \chi & k = -1 \end{cases}. \quad (2.6)$$

The metric of Eq. (2.5) is valid for  $\chi > \chi_0$ , with  $\chi_0$  denoting the comoving position of  $\Sigma$ . The behavior of the scale factor is determined by the spatial curvature and the matter content of the universe. Here we assume that the universe is matter dominated, with a stress-energy tensor given by  $T^{\alpha\beta} = \rho u^\alpha u^\beta$ , where  $\rho$  is the dust's mass density and  $u^\alpha = a^{-1} \partial x^\alpha / \partial \eta$  its four-velocity. Conservation of energy implies that  $\rho a^3 = \text{constant} \equiv 3C/(8\pi)$ . By virtue of the Einstein field equations, the scale factor must satisfy  $a'^2 + ka^2 = Ca$ , in which a prime indicates differentiation with respect to  $\eta$ . Proper time for comoving observers is obtained by integrating  $d\tau = a(\eta) d\eta$ .

For spatial sections with positive curvature ( $k = 1$ ), the scale factor and the proper time are given by

$$a(\eta) = \frac{C}{2} (1 - \cos \eta), \quad \tau(\eta) = \frac{C}{2} (\eta - \sin \eta), \quad (2.7)$$

where  $C = 8\pi\rho a^3/3$  is a constant. For spatial sections with negative curvature ( $k = -1$ ), we have instead

$$a(\eta) = \frac{C}{2} (\cosh \eta - 1), \quad \tau(\eta) = \frac{C}{2} (\sinh \eta - \eta). \quad (2.8)$$

Finally, for flat spatial sections ( $k = 0$ ) we have

$$a(\eta) = \frac{C}{4} \eta^2, \quad \tau(\eta) = \frac{C}{12} \eta^3. \quad (2.9)$$

The metrics of Eq. (2.1) and (2.2) must be matched at their common boundary [23], the timelike hypersurface  $\Sigma$  described by  $r = r_{\Sigma}(\tau)$  on the Schwarzschild side, and  $\chi = \chi_0$  on the FLRW side. The boundary's induced metric, as seen from the interior, is

$$ds_{\Sigma}^2 = -d\tau^2 + [r_{\Sigma}(\tau)]^2 d\Omega^2. \quad (2.10)$$

As seen from the exterior, it is

$$ds_{\Sigma}^2 = -d\tau^2 + [a(\tau)s(\chi_0)]^2 d\Omega^2. \quad (2.11)$$

In both cases the induced metric is expressed in terms of the hypersurface's intrinsic coordinates  $(\tau, \theta, \phi)$ , with  $\tau$  denoting proper time for observers comoving with the hypersurface. Equality of the induced metric on both sides of the hypersurface implies

$$r_{\Sigma}(\tau) = a(\tau)s(\chi_0), \quad (2.12)$$

in which  $r_{\Sigma}(\tau)$  is given implicitly by Eqs. (2.2), (2.3), or (2.4), while  $a(\tau)$  is given implicitly by Eqs. (2.7), (2.8), or (2.9). These equations are compatible with Eq. (2.12) provided that the relations

$$\tilde{E} = \frac{ds}{d\chi}(\chi_0) \quad (2.13)$$

and

$$M = \frac{1}{2} C s^3(\chi_0) = \frac{4\pi}{3} \rho a^3 s^3(\chi_0) \quad (2.14)$$

hold. Equation (2.14) implies that the mass of the black hole is equal to the mass removed from the interior of  $\Sigma$ , as was said previously. It can be checked that Eqs. (2.12) and (2.13) ensure the continuity of the extrinsic curvature across  $\Sigma$ : the union of the Schwarzschild and FLRW metrics forms a globally valid solution to the Einstein field equations [23].

## B. Double-null coordinates

The metric of the Einstein-Straus spacetime has thus far been expressed in terms of two coordinate patches. We now construct a single coordinate system  $(u, v, \theta, \phi)$  that covers both regions of the spacetime. These coordinates are null, and in the cosmological region they are defined by

$$u = \eta - \chi, \quad v = \eta + \chi. \quad (2.15)$$

They are related to similar coordinates that can be introduced in the Schwarzschild region,

$$\bar{u} = t - r^*, \quad \bar{v} = t + r^*, \quad (2.16)$$

where  $r^* = \int f^{-1} dr = r + 2M \ln(r/2M - 1)$ . The relations  $\bar{u}(u)$ ,  $\bar{v}(v)$  can be obtained by using these coordinates to express continuity of the induced metric across  $\Sigma$ .

For example, equating the  $ds_{\Sigma}^2$  of Eq. (2.11), expressed in terms of  $d\bar{v}$ , to the  $ds_{\Sigma}^2$  of Eq. (2.10), expressed in terms of  $dv$ , yields

$$(1 - 2M/r_{\Sigma})d\bar{v}^2 - 2dr_{\Sigma}d\bar{v} = a^2 dv^2. \quad (2.17)$$

Here, the scale factor must be expressed as a function of  $v - \chi_0$ , and  $r_\Sigma$  is viewed as the function of  $v$  defined by Eq. (2.12). Equation (2.17) is a quadratic equation for  $d\bar{v}/dv$ . Solving this, using Eq. (2.14), gives

$$\frac{d\bar{v}}{dv} = \frac{a's_0 + a\sqrt{1 - ks_0^2}}{1 - Cs_0^2/a}, \quad (2.18)$$

where a prime indicates differentiation with respect to  $v - \chi_0$ ,  $s_0 \equiv s(\chi_0)$ , and  $C = 8\pi\rho a^3/3$ . More explicitly, substituting Eqs. (2.6), (2.7), and (2.14) into Eq. (2.18) yields

$$\frac{d\bar{v}}{dv} = \frac{M}{\sin^3 \chi_0} \frac{[1 - \cos(v - \chi_0)][\cos \chi_0 - \cos v]}{\cos(2\chi_0) - \cos(v - \chi_0)} \quad (2.19)$$

for  $k = 1$ . Similarly, substituting Eqs. (2.6), (2.8), and (2.14) into Eq. (2.18) yields

$$\frac{d\bar{v}}{dv} = \frac{M}{\sinh^3 \chi_0} \frac{[\cosh(v - \chi_0) - 1][\cosh v - \cosh \chi_0]}{\cosh(v - \chi_0) - \cosh(2\chi_0)} \quad (2.20)$$

for  $k = -1$ . Finally, using Eq. (2.9) instead gives

$$\frac{d\bar{v}}{dv} = \frac{M}{2\chi_0^3} \frac{(v - \chi_0)^3}{v - 3\chi_0} \quad (2.21)$$

for  $k = 0$ . These relations for  $d\bar{v}/dv$  go to zero at  $v = \chi_0$ , which represents the past singularity of the cosmological spacetime, and they are singular at  $v = 3\chi_0$ , which represents the extension of the black hole's past horizon into the cosmological region (see Fig. 1).

A nearly identical set of calculations gives us the relations  $\bar{u}(u)$ . Here we find

$$\frac{d\bar{u}}{du} = \frac{M}{\sin^3 \chi_0} \frac{[1 - \cos(u + \chi_0)][\cos \chi_0 - \cos u]}{\cos(2\chi_0) - \cos(u + \chi_0)} \quad (2.22)$$

for  $k = 1$ ,

$$\frac{d\bar{u}}{du} = \frac{M}{\sinh^3 \chi_0} \frac{[\cosh(u + \chi_0) - 1][\cosh u - \cosh \chi_0]}{\cosh(u + \chi_0) - \cosh(2\chi_0)} \quad (2.23)$$

for  $k = -1$ , and

$$\frac{d\bar{u}}{du} = \frac{M}{2\chi_0^3} \frac{(u + \chi_0)^3}{u + 3\chi_0} \quad (2.24)$$

for  $k = 0$ .

Equations (2.19)–(2.24) can all be integrated in closed form. For  $k = \pm 1$ , the resulting expressions for  $\bar{v}(v)$  and  $\bar{u}(u)$  are quite complicated, and we shall not display them here. For  $k = 0$  the relations are simple, and we find

$$\bar{v} = M \left[ \frac{1}{6} \left( \frac{v}{\chi_0} \right)^3 + \frac{3}{2} \left( \frac{v}{\chi_0} \right) + 4 \ln \left( \frac{v}{\chi_0} - 3 \right) - \left( \frac{10}{3} + 8 \ln 2 \right) \right] \quad (2.25)$$

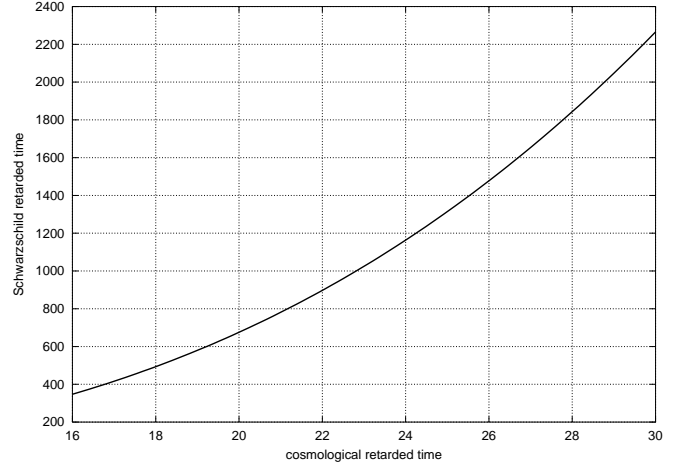


FIG. 2. The relationship between the cosmological retarded-time coordinate  $u$  and the Schwarzschild retarded-time coordinate  $\bar{u}$ . The plot is constructed for the interval  $16 < u < 30$ , choosing  $\chi_0 = 1$  and setting  $2M \equiv 1$ . A graph of  $\bar{v}(v)$  would be almost identical for these choices of parameters.

and

$$\bar{u} = M \left[ \frac{1}{6} \left( \frac{u}{\chi_0} \right)^3 + \frac{3}{2} \left( \frac{u}{\chi_0} \right) - 4 \ln \left( \frac{u}{\chi_0} + 3 \right) \right]. \quad (2.26)$$

We have tuned the constants of integration to produce agreement between Eqs. (2.25) and (2.26) and the defining relation  $\frac{1}{2}(\bar{v} - \bar{u}) = r + 2M \ln(r/2M - 1)$ ; the right-hand side must be evaluated on  $\Sigma$  and expressed in terms of  $u$  and  $v$  by means of Eq. (2.12). The relation  $\bar{u}(u)$  is plotted in Fig. 2; the relation between  $\bar{v}$  and  $v$  is nearly identical.

Both sides of the Einstein-Straus spacetime can be covered by the single coordinate system  $(u, v, \theta, \phi)$  constructed above. Our coordinates, however, do not extend beyond the future horizon of the Schwarzschild region. As far as we are aware, this coordinate system was never presented before in the literature.

### III. SCALAR WAVE EQUATION

We consider the propagation of a scalar field  $\Phi$  in the Einstein-Straus spacetime. This field satisfies the wave equation

$$(\square - \xi R)\Phi = 0, \quad (3.1)$$

in which  $\square = g^{\alpha\beta} \nabla_\alpha \nabla_\beta$  is the curved-spacetime d'Alembertian operator,  $R$  the Ricci scalar, and  $\xi$  an arbitrary dimensionless constant; the scalar field is minimally coupled to curvature if  $\xi = 0$ , and it is conformally coupled if  $\xi = \frac{1}{6}$ .

In the cosmological region, where the metric is given by Eq. (2.5), we separate the variables by writing

$$\Phi(\eta, \chi, \theta, \phi) = \frac{1}{a(\eta)s(\chi)} \sum_{lm} \psi_l(\eta, \chi) Y_{lm}(\theta, \phi). \quad (3.2)$$

Here,  $Y_{lm}(\theta, \phi)$  are the usual spherical harmonics, and  $\psi_l(\eta, \chi)$  is a reduced wave function that satisfies

$$\left[ -\frac{\partial^2}{\partial \eta^2} + \frac{\partial^2}{\partial \chi^2} + \frac{1-6\xi}{2a(\eta)/C} - \frac{l(l+1)}{s^2(\chi)} \right] \psi_l = 0, \quad (3.3)$$

where  $2a(\eta)/C$  and  $s(\chi)$  are respectively equal to  $1 - \cos \eta$  and  $\sin \chi$  if  $k = -1$ ,  $\cosh \eta - 1$  and  $\sinh \chi$  if  $k = 1$ , and  $\frac{1}{2}\eta^2$  and  $\chi$  if  $k = 0$ .

In the Schwarzschild region, where the metric is given by Eq. (2.1), we let

$$\Phi(t, r, \theta, \phi) = \frac{1}{r} \sum_{lm} \psi_l(t, r) Y_{lm}(\theta, \phi). \quad (3.4)$$

The reduced wave function now satisfies

$$\left\{ -\frac{\partial^2}{\partial t^2} + \frac{\partial^2}{\partial r^{*2}} - f \left[ \frac{l(l+1)}{r^2} + \frac{2M}{r^3} \right] \right\} \psi_l = 0, \quad (3.5)$$

where  $r^* = r + 2M \ln(r/2M - 1)$  and  $f = 1 - 2M/r$ .

The field  $\Phi$  and its derivatives  $\Phi_{,\alpha}$  are continuous across the boundary separating the Schwarzschild and cosmological regions. Smoothness of the metric across  $\Sigma$  ensures that the reduced wave function  $\psi_l$  and its derivatives are also continuous at the boundary.

Using the coordinates  $u$  and  $v$  introduced in Sec. II B, the reduced wave equation becomes

$$\frac{\partial^2 \psi_l}{\partial u \partial v} = -\frac{1}{4} V_l(u, v) \psi_l \quad (3.6)$$

on both sides of the boundary. The effective potential  $V_l(u, v)$  takes a different form in the two portions of the spacetime. In the cosmological region, it is

$$V_l^{\text{out}} = \frac{l(l+1)}{s^2(\chi)} - \frac{1-6\xi}{2a(\eta)/C}, \quad (3.7)$$

where  $\eta = \frac{1}{2}(v+u)$  and  $\chi = \frac{1}{2}(v-u)$ . In the Schwarzschild region, we have instead

$$V_l^{\text{in}} = \frac{d\bar{u}}{du} \frac{d\bar{v}}{dv} \left( 1 - \frac{2M}{r} \right) \left[ \frac{l(l+1)}{r^2} + \frac{2M}{r^3} \right], \quad (3.8)$$

in which  $r(u, v)$  is defined implicitly by  $r^* = \frac{1}{2}(\bar{v} - \bar{u})$ ; the relations  $\bar{u}(u)$  and  $\bar{v}(v)$  were obtained at the end of Sec. II B. It should be noted that the potential is *discontinuous* at the boundary; this is explained by the fact that the density  $\rho$  is discontinuous at  $\Sigma$ .

The reduced wave equation, in the form of Eq. (3.6), can be straightforwardly integrated on both sides of  $\Sigma$ , which is described by the relation  $v = u + 2\chi_0$ . The initial data required for a unique solution consists of  $\psi_l(u, v = v_0)$  and  $\psi_l(u = u_0, v)$ , the value of the wave function on the two null surfaces  $v = v_0$  and  $u = u_0$ ; these values can be specified freely.

## IV. NUMERICAL RESULTS

We now present our numerical integrations of Eq. (3.6). The algorithm used for this task is based on the finite-difference scheme suggested by Gundlach, Price, and Pullin [11]. In this scheme, the  $(u, v)$  continuum is discretized in units of  $\Delta$ , and Eq. (3.6) is replaced by the approximation

$$\psi_l(u + \Delta, v + \Delta) = \left[ 1 - \frac{1}{8} V_l \Delta^2 + O(\Delta^4) \right] \left[ \psi_l(u + \Delta, v) + \psi_l(u, v + \Delta) \right] - \psi_l(u, v), \quad (4.1)$$

in which the potential is evaluated at the off-grid point  $(u + \frac{1}{2}\Delta, v + \frac{1}{2}\Delta)$ . For simplicity we restrict our attention to spatially-flat cosmologies ( $k = 0$ ), and a scalar field that is minimally coupled to curvature ( $\xi = 0$ ). In Eq. (3.7) we must therefore substitute  $s(\chi) = \chi = \frac{1}{2}(v-u)$  and  $2a(\eta)/C = \frac{1}{2}\eta^2 = \frac{1}{8}(v+u)^2$ . In Eq. (3.8), the relations  $\bar{v}(v)$  and  $\bar{u}(u)$  are obtained from Eq. (2.25) and (2.26), respectively; their derivatives are given by Eqs. (2.21) and (2.24). For the initial value of the wave function on  $u = u_0$  we choose a gaussian wave packet of width  $\sigma$  centered at  $v = v_c$ :

$$\psi_l(u = u_0, v) = \exp \left[ -\frac{(v - v_c)^2}{2\sigma^2} \right]. \quad (4.2)$$

On  $v = v_0$  we make the choice  $\psi_l(u, v = v_0) = \psi_l(u_0, v_0) \simeq 0$ : the initial field is a purely ingoing wave packet.

The parameter space associated with the numerical integration of Eq. (3.6) is rather large, but moving in this space does not affect the qualitative aspects of the wave's evolution. For concreteness we set  $\chi_0 = 1$ ,  $2M = 1$ ,  $u_0 = 17$ ,  $v_0 = 16$ ,  $v_c = 16.9$ ,  $\sigma = 0.2$ . These choices ensure that the initial wave packet is contained entirely within the Schwarzschild region of the spacetime; its center is located in the strong-field region near  $r^* = 0$ . The discretization unit  $\Delta$  must be set sufficiently small to ensure that the potential  $V_l$  in Eq. (4.1) is well sampled. In our simulations we use  $\Delta = 0.001$ ; choosing a smaller value does not appreciably change our results. In Fig. 3 we display the numerical grid and a few relevant features of the spacetime.

Equation (4.1) is used to numerically evolve  $\psi_l$  from the initial conditions imposed on the lines  $u = 17$  and  $v = 16$ . The wave function is then evaluated on three different curves of the  $(u, v)$  plane. The first is the line  $u = 30$ , which approximates the black hole's event horizon (see Fig. 3); there  $\psi_l$  is expressed as a function of cosmological advanced time  $v$ . The second is the line  $v = u + 2$ , which represents the boundary  $\Sigma$ ; there  $\psi_l$  is expressed as a function of conformal time  $\eta = v - 1 = u + 1$ . The third is the line  $v = 30$ , which approximates future null infinity (see Fig. 3); there  $\psi_l$  is expressed as a function of cosmological retarded time  $u$ .

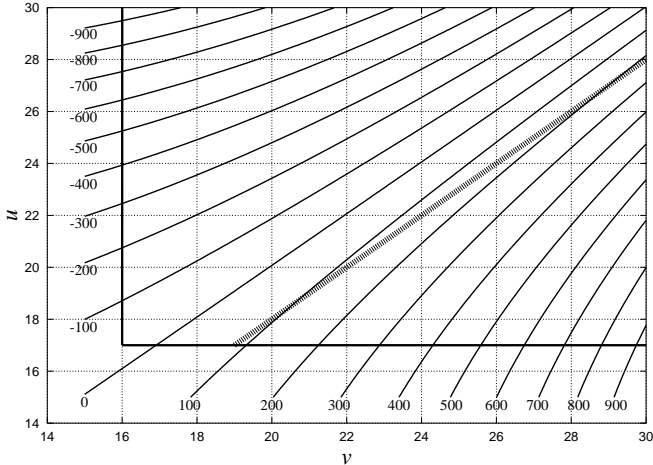


FIG. 3. The portion of the Einstein-Straus spacetime that is relevant for our numerical integrations. With  $\chi_0 = 1$ , this corresponds to the intervals  $17 < u < 30$  and  $16 < v < 30$ . The thick, dashed line described by  $v = u + 2$  represents the boundary  $\Sigma$ . The Schwarzschild region of the spacetime appears above the boundary, while the FLRW region appears below. The solid lines are curves  $r^*(u, v) = \text{constant}$ , with the label giving the value of the constant (in units  $2M = 1$ ); these curves are meaningful only in the Schwarzschild part of the spacetime. Notice that the curve  $r^* = 0$  is well approximated by  $v = u$ . The initial wave packet on  $u = 17$  is centered at  $v = 16.9$ , at which  $r^* \simeq 0$ ; it is therefore located in the strong-field region of the Schwarzschild spacetime. Because  $r^*$  is negatively large everywhere on  $u = 30$ , this surface closely approximates the black hole’s event horizon. We similarly take  $v = 30$  to approximate future null infinity, although the approximation becomes poor as  $u$  increases.

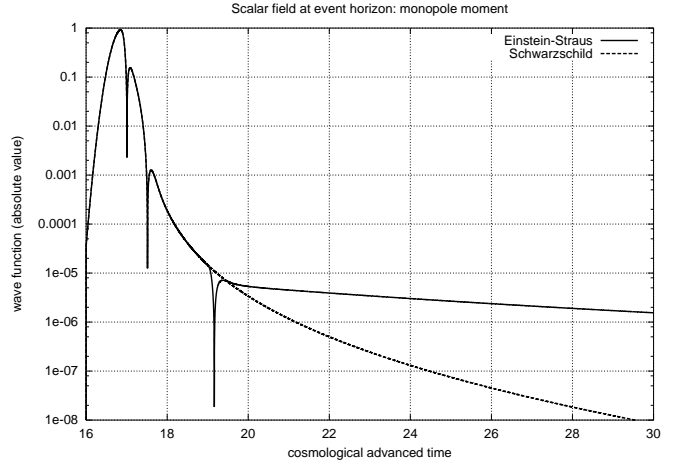


FIG. 4. A plot of  $|\psi_0(u = 30)|$ , the absolute value of the  $l = 0$  wave function on the event horizon, as a function of cosmological advanced time  $v$ . Prior to  $v = 19$ , the wave behaves as it would in Schwarzschild spacetime. This early-time behavior is characterized by quasi-normal oscillations (which on a logarithmic scale are revealed by deep troughs) and the onset of inverse power-law falloff. At  $v = 19$  the field comes in causal contact with the cosmological region and suddenly alters its behavior. The wave function changes sign, and it subsequently falls off at a much slower rate; as we show in Sec. V, this late-time behavior is not well described by an inverse power-law.

The results of our numerical simulations are displayed in Figs. 4–12, and the captions describe the graphs in detail. In the following paragraphs we describe and explain the salient features.

Wave propagation in the Einstein-Straus spacetime is governed by the potential  $V_l$  displayed in Eqs. (3.7) and (3.8). The most important aspects of this potential are that it peaks near  $r^* = 0$  (because of the strong curvature near the black hole) and that it is discontinuous at the boundary (because of the jump in the density  $\rho$ ). For the purposes of understanding the gross properties of the wave’s evolution, the potential can be thought of as consisting of a narrow barrier near  $r^* = 0$  and a jump discontinuity at  $\chi = \chi_0$ . After each encounter with the barrier or the jump, the wave is partially transmitted and reflected, and these processes determine the late-time behavior of the scalar field. The diagram of Fig. 3 informs us that the curve  $r^* = 0$  is well approximated by the line  $v = u$ . The potential barrier is therefore located near  $v = u$ , while the jump discontinuity is at  $v = u + 2$ .

Consider, as we do in our numerical simulations, an initially ingoing wave packet on  $u = 17$ , centered at  $v = 16.9$ . In the absence of any potential, the wave would keep its shape as it moves toward increasing values of  $u$ . In the diagram of Fig. 3, the wave packet would move vertically upward, and it would eventually register on the “event horizon” at  $u = 30$ ; the wave profile on  $u = 30$  would be identical to the initial configuration on  $u =$

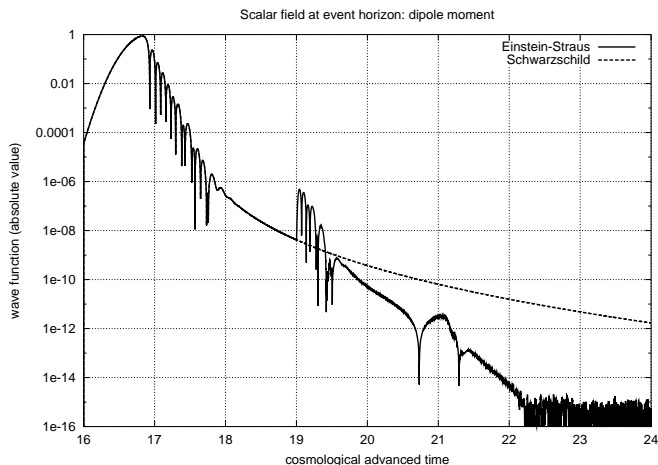


FIG. 5. A plot of  $|\psi_1(u = 30)|$ , the absolute value of the  $l = 1$  wave function on the event horizon, as a function of cosmological advanced time  $v$ . The early-time behavior is again characterized by quasi-normal oscillations (with a higher frequency and a faster decay time than the  $l = 0$  case) and the onset of inverse power-law falloff. At  $v = 19$  a faint echo of the early-time signal registers on the event horizon. A second echo also appears near  $v = 21$ . Beyond  $v = 22$ , the wave function drops below  $10^{-15}$  and our numerical results become unreliable.

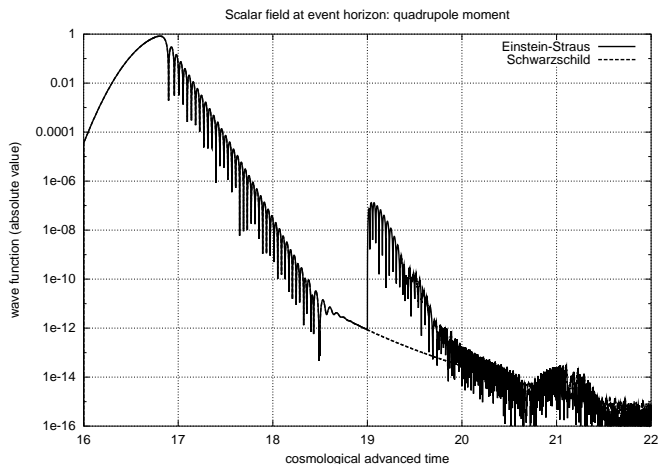


FIG. 6. A plot of  $|\psi_2(u = 30)|$ , the absolute value of the  $l = 2$  wave function on the event horizon, as a function of cosmological advanced time  $v$ . Again we have quasi-normal oscillations and inverse power-law falloff at early times, followed by echoes of the early signal at later times. Our numerical results become noisy beyond  $v = 20$ , but a second echo can still be seen near  $v = 21$ .

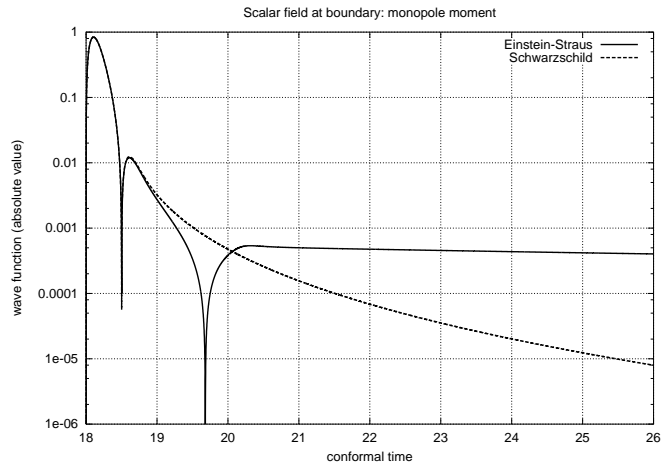


FIG. 7. A plot of  $|\psi_0(v = u + 2)|$ , the absolute value of the  $l = 0$  wave function on the boundary  $\Sigma$ , as a function of conformal time  $\eta$ . At early times the field behaves as it would in Schwarzschild spacetime. At later times, from  $\eta = 19$  onward, the multiple reflections from the potential barrier near  $r^* = 0$  and the jump discontinuity at  $\Sigma$  alter the behavior of the wave function. At  $\eta \simeq 19.7$ , the wave function changes sign, and it subsequently falls off at a slow rate; as we show in Sec. V, this behavior is not well described by an inverse power-law.

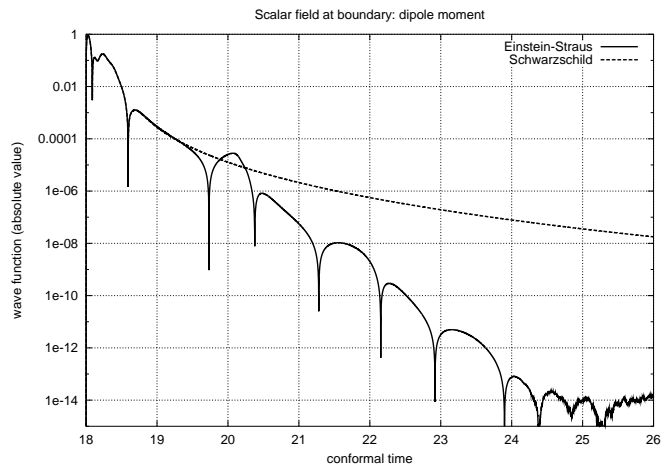


FIG. 8. A plot of  $|\psi_1(v = u + 2)|$ , the absolute value of the  $l = 1$  wave function on the boundary  $\Sigma$ , as a function of conformal time  $\eta$ . Again we have Schwarzschild-type behavior at early times, and strong deviations from it starting at  $\eta = 19$ . The multiple reflections of the wave packet give rise to the oscillatory behavior seen in the figure. The period of these oscillations is approximately  $\Delta\eta \simeq 2$ , twice the light-travel time between the boundary and the potential barrier. (At first glance, the frequency appears to be twice as large because the repeated pattern, which can be seen in the interval  $18 < \eta < 19$ , already contains a sign change.) The end result is a field that decays faster than in Schwarzschild spacetime, contrary to what takes place for  $l = 0$ . Our numerical results become unreliable beyond  $\eta = 24$ .

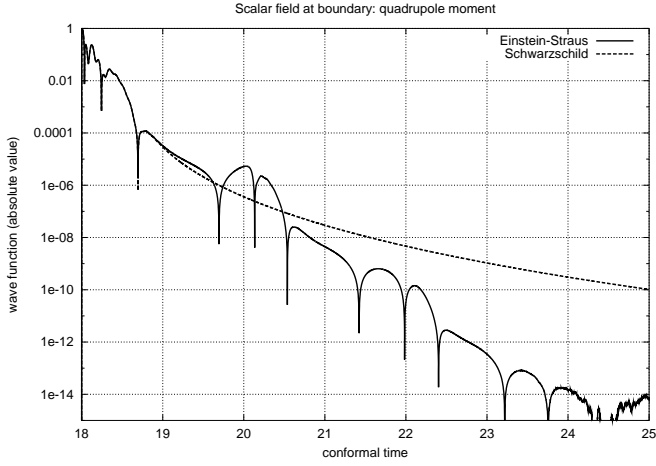


FIG. 9. A plot of  $|\psi_2(v = u + 2)|$ , the absolute value of the  $l = 2$  wave function on the boundary  $\Sigma$ , as a function of conformal time  $\eta$ . We recognize the late-time oscillatory behavior that was identified in Fig. 8. Here also the field decays faster than it would in Schwarzschild spacetime. Our numerical results become unreliable beyond  $\eta = 24$ .

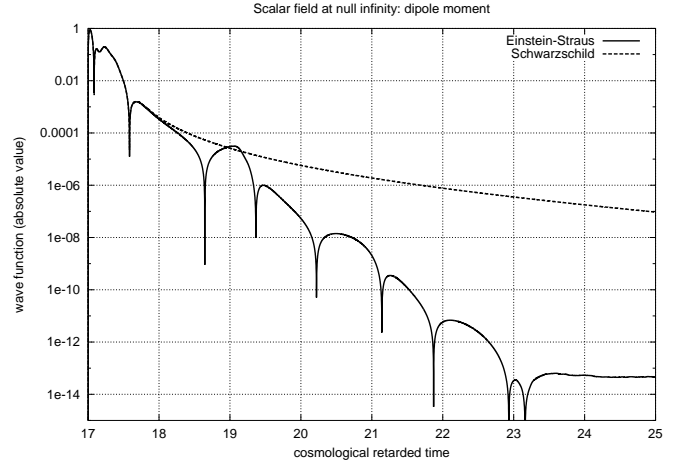


FIG. 11. A plot of  $|\psi_1(v = 30)|$ , the absolute value of the  $l = 1$  wave function at future null infinity, as a function of cosmological retarded time  $u$ . The behavior seen here is more or less a direct image of what was already seen at the boundary, in Fig. 8. Contrary to the  $l = 0$  case, the field decays faster in the Einstein-Straus spacetime than in Schwarzschild spacetime.

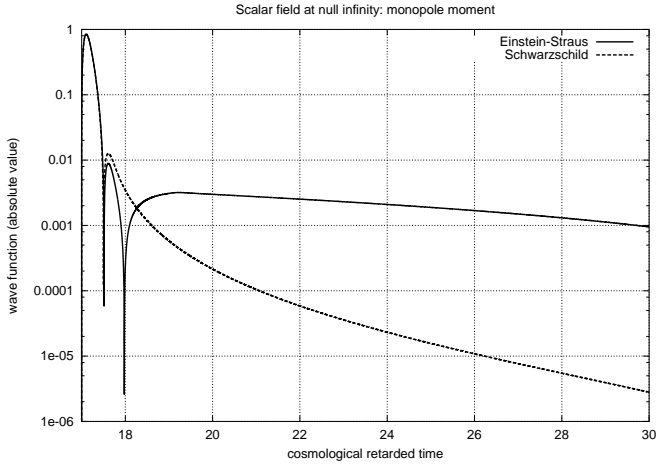


FIG. 10. A plot of  $|\psi_0(v = 30)|$ , the absolute value of the  $l = 0$  wave function at future null infinity, as a function of cosmological retarded time  $u$ . The behavior seen here is more or less a direct image of what was already seen at the boundary, in Fig. 7. Compared with the Schwarzschild behavior, the field decays at a slower rate; as we show in Sec. V, this behavior is not well described by an inverse power-law.

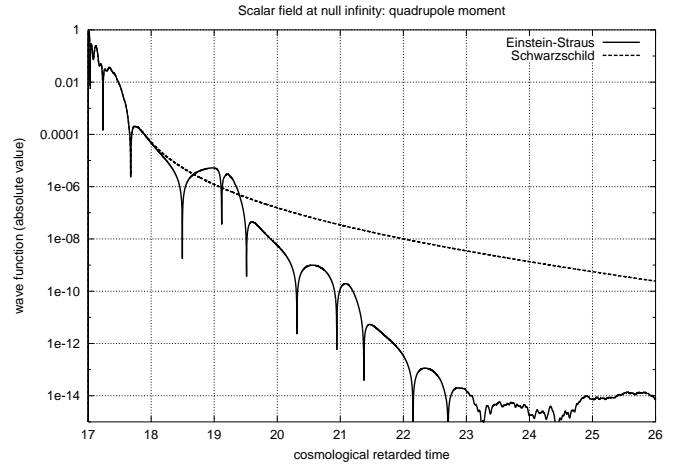


FIG. 12. A plot of  $|\psi_2(v = 30)|$ , the absolute value of the  $l = 2$  wave function at future null infinity, as a function of cosmological retarded time  $u$ . The behavior seen here is more or less a direct image of what was already seen at the boundary, in Fig. 9. Compared with its Schwarzschild behavior, the field decays at a faster rate.

17. Instead, our wave packet moves in the presence of the potential, which produces partial transmissions and reflections as well as distortions in the packet's shape.

Because the initial wave packet is centered near  $r^* = 0$ , it almost immediately encounters the potential barrier as it propagates away from  $u = 17$ . The partially transmitted wave moves vertically upward in the diagram of Fig. 3, and a distorted wave profile registers on the event horizon; this profile still has a recognizable center at  $v = 16.9$ . On the other hand, the partially reflected wave moves horizontally toward the right, and it soon arrives at the boundary; the center of the wave packet arrives shortly after  $\eta = u_0 + 1 = 18$ .

At the boundary, the right-moving wave encounters the jump in the potential and undergoes partial transmission and reflection. The transmitted wave proceeds toward future null infinity without much further distortion; the center of the wave packet arrives shortly after  $u = u_0 = 17$ . On the other hand, the reflected wave moves vertically upward in the diagram, and the center of the packet follows the line  $v = \eta_0 + 1 = 19$ . It encounters once more the potential barrier near  $u = v$ .

At the barrier, the up-moving wave is partially transmitted and reflected. The transmitted wave continues along  $v = 19$  and it finally registers on the event horizon, where it is recognized as a faint echo of the original signal. The reflected wave moves horizontally along  $u = 19$ , and proceeds toward the jump at  $v = u + 2$ . There the entire cycle of partial transmissions and reflections repeats once more.

In the figures, the behavior of the wave function in the Einstein-Straus spacetime is contrasted with the behavior it would have in Schwarzschild spacetime. Because the scalar field is at first causally disconnected from the cosmological region, the early-time behaviors coincide. As the field comes in causal contact with the boundary and the expanding universe beyond it, its behavior changes. In particular, the inverse power-law falloff witnessed at late times for Schwarzschild spacetime is not seen in the Einstein-Straus spacetime. Instead, the field's late-time behavior is quite complicated, and governed by many cycles of partial transmissions and reflections, as was described above.

## V. PARTIAL TRANSMISSIONS AND REFLECTIONS: A TOY MODEL

In this final section we firm up the claim made in Sec. IV that late-time wave propagation in the Einstein-Straus spacetime is governed mostly by partial transmissions and reflections. We recall that these are produced by the most important features of the potential  $V_l$ : a fairly well localized barrier near  $r^* = 0$  and a jump discontinuity at the boundary  $\Sigma$ . To explore the physics of those transmissions and reflections, we consider a toy model involving a simpler potential that still captures the

essential features of the original potential. The new wave equation is sufficiently simple that we will be able to find an analytical solution.

### A. Formulation of the toy model

The toy model is based on the wave equation

$$\left(-\frac{\partial^2}{\partial \eta^2} + \frac{\partial^2}{\partial \chi^2} - V\right)\psi = 0, \quad (5.1)$$

in which the potential is given by

$$V(\eta, \chi) = \begin{cases} 0 & 0 < \chi < \chi_0 \\ -2/\eta^2 & \chi > \chi_0 \end{cases}. \quad (5.2)$$

The potential vanishes on the left-hand side of the boundary at  $\chi = \chi_0$ , and the wave propagates freely in the interval  $0 < \chi < \chi_0$ . This interval is our model for the region between the potential barrier near  $r^* = 0$  and the boundary  $\Sigma$ : we effectively “switch off” the potential in the Schwarzschild region of the spacetime. The partial reflections off the potential barrier are replaced by total reflections at  $\chi = 0$ , where we impose the boundary condition

$$\psi(\eta, \chi = 0) = 0. \quad (5.3)$$

On the right-hand side of the boundary, for  $\chi > \chi_0$ , the potential is  $\eta$ -dependent, a behavior that is inherited by taking the special case  $l = 0$ ,  $\xi = 0$ , and  $2a(\eta)/C = \frac{1}{2}\eta^2$  of Eq. (3.7). For  $\chi > \chi_0$ , therefore, Eq. (5.1) describes a  $l = 0$ , minimally-coupled wave propagating in a spatially-flat cosmology. Notice that for  $\chi < \chi_0$ , Eq. (5.1) describes a  $l = 0$  wave propagating in flat spacetime.

The toy model incorporates an infinite potential barrier at  $\chi = 0$  and a jump discontinuity at  $\chi = \chi_0$ . We believe that this is sufficient to capture, in the simplest possible way, the essential features of wave propagation in the Einstein-Straus spacetime. The toy model, however, does not incorporate an event horizon, and it does not take into account the effect of the  $l(l+1)$  part of the potential.

In the rest of the section we will integrate Eq. (5.1) analytically, subjected to the initial conditions

$$\psi(u, v_0) = f(u), \quad \psi(u_0, v) = 0, \quad (5.4)$$

where  $f(u)$  is a specified function with support in the interval  $v_0 < u < u_0$ ; this corresponds to an initially *outgoing* wave packet. We have re-introduced the null coordinates  $u$  and  $v$ , related to the original coordinates by  $u = \eta - \chi$ ,  $v = \eta + \chi$ . We will be interested mostly in the behavior of the wave function at  $\chi = \chi_0$ . We sketch the evolution of the wave packet in Fig. 13.

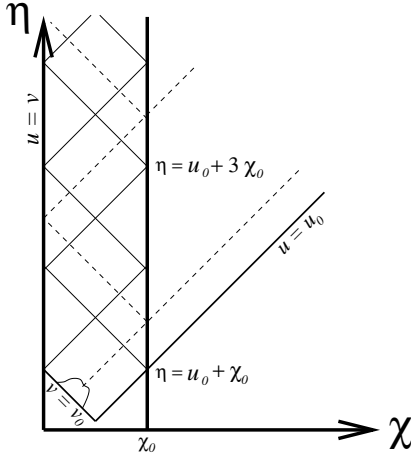


FIG. 13. Wave propagation in the toy model. The diagram sketches the evolution of the initial wave packet, which is placed on the line  $v = v_0$ . When it first reaches the boundary at  $\chi = \chi_0$ , the wave is partially transmitted and reflected. The reflected wave moves back toward  $\chi = 0$ , where it is totally reflected. The new outgoing wave encounters once more the boundary, and it is again partially transmitted and reflected. The entire cycle repeats *ad infinitum*. The first epoch of wave propagation refers to the wave's first encounter with the boundary; it begins at  $\eta = u_0 + \chi_0$  and ends at  $\eta = u_3 + 3\chi_0$ . The second epoch refers to the wave's second encounter with the boundary; it begins at  $\eta = u_0 + 3\chi_0$  and ends at  $\eta = u_3 + 5\chi_0$ .

## B. Elementary solutions

We shall impose that  $\psi$  and its derivative with respect to  $\chi$  be continuous at  $\chi = \chi_0$ . This will allow us to describe the partial transmissions and reflections that take place at the boundary. The total reflections occurring at  $\chi = 0$  are described by Eq. (5.3). The difficulty of the forthcoming calculations resides entirely with the imposition of these matching conditions. Solving the wave equation separately in the two domains  $\chi < \chi_0$  and  $\chi > \chi_0$  is, by contrast, quite trivial. For  $V = 0$ , the general solution to Eq. (5.1) is

$$\psi_{\text{left}} = a(u) + b(v), \quad (5.5)$$

in which  $a$  and  $b$  are arbitrary functions of their arguments. For  $V = -2/\eta^2$ , the general solution to Eq. (5.1) is

$$\psi_{\text{right}} = \left( \frac{d}{du} - \frac{1}{\eta} \right) A(u) + \left( \frac{d}{dv} - \frac{1}{\eta} \right) B(v), \quad (5.6)$$

in which  $A$  and  $B$  are arbitrary functions of their arguments.

We note in passing that Eqs. (5.5) and (5.6) can easily be generalized to potentials that include a  $l(l+1)/\chi^2$  term. Starting from a monopole solution  $\psi_0$ , a dipole ( $l = 1$ ) solution is obtained by letting  $\psi_1 = (-\partial/\partial\chi + 1/\chi)\psi_0$ , and a quadrupole ( $l = 2$ ) solution is obtained by letting

$\psi_2 = (-\partial/\partial\chi + 2/\chi)\psi_1$ . The general rule is that a  $(l+1)$ -pole solution is obtained from a  $l$ -pole solution by letting  $\psi_{l+1} = [-\partial/\partial\chi + (l+1)/\chi]\psi_l$ .

## C. Matching: First epoch

We begin by matching the solutions (5.5) and (5.6) in the interval  $u_0 + \chi_0 < \eta < u_0 + 3\chi_0$ . During this *first epoch*, the following events take place: (i) the initially outgoing wave packet represented by  $f(u)$  arrives at  $\chi = \chi_0$  and is partially transmitted and reflected; (ii) the reflected wave moves back toward  $\chi = 0$  and is totally reflected there; (iii) the new outgoing wave, which later will be represented by the function  $f_{\text{new}}(u)$ , starts to move toward  $\chi = \chi_0$ . The first epoch, therefore, includes only the first interaction between the outgoing wave and the boundary.

During the first epoch,

$$\psi_{\text{left}} = f(u) + g(v), \quad (5.7)$$

where  $f(u)$  represents the initially outgoing wave packet, and  $g(v)$  its partial reflection off the boundary; we have  $g(v) = 0$  for  $v < u_0 + 2\chi_0$ . On the other hand,

$$\psi_{\text{right}} = \dot{F}(u) - \frac{1}{\eta} F(u), \quad (5.8)$$

and this represents the wave that is partially transmitted across the boundary; an overdot indicates differentiation with respect to  $u$ . The functions  $g(v)$  and  $F(u)$  are determined by imposing continuity of  $\psi$  and  $\psi_{,\chi}$  across  $\chi = \chi_0$ . The equation that determines  $F(u)$  is

$$\dot{F}(u) - \frac{\dot{F}(u)}{u + \chi_0} + \frac{F(u)}{2(u + \chi_0)^2} = \dot{f}(u). \quad (5.9)$$

The equation that determines  $g(v)$  is

$$g(v) = -f(v - 2\chi_0) + \dot{F}(v - 2\chi_0) - \frac{F(v - 2\chi_0)}{v - \chi_0}. \quad (5.10)$$

We must first integrate Eq. (5.9) subjected to the initial conditions  $F(u_0) = \dot{F}(u_0) = 0$ . Standard integration techniques [24] reveal that the required solution is

$$F(u) = \frac{1}{2}(u + \chi_0)^{1+\gamma} \int_{u_0}^u \frac{f(u')}{(u' + \chi_0)^{1+\gamma}} du' + \frac{1}{2}(u + \chi_0)^{1-\gamma} \int_{u_0}^u \frac{f(u')}{(u' + \chi_0)^{1-\gamma}} du', \quad (5.11)$$

where  $\gamma \equiv 1/\sqrt{2}$ . Substituting this into Eq. (5.10) gives

$$g(v) = \frac{\gamma}{2}(v - \chi_0)^\gamma \int_{u_0+2\chi_0}^v \frac{f(v' - 2\chi_0)}{(v' - \chi_0)^{1+\gamma}} dv' - \frac{\gamma}{2}(v - \chi_0)^{-\gamma} \int_{u_0+2\chi_0}^v \frac{f(v' - 2\chi_0)}{(v' - \chi_0)^{1-\gamma}} dv'. \quad (5.12)$$

We recall that this ingoing wave is totally reflected at  $\chi = 0$ , and that it becomes the new outgoing wave  $f_{\text{new}}(u) = -g(v)$ .

By substituting Eq. (5.11) into Eq. (5.8) or Eq. (5.12) into Eq. (5.7), we finally obtain the wave function  $\psi(u, v)$ . Its expression on the boundary is

$$\begin{aligned} \psi(\eta, \chi_0) = & f(\eta - \chi_0) + \frac{\gamma}{2} \eta^\gamma \int_{u_0 + \chi_0}^{\eta} \frac{f(\eta' - \chi_0)}{\eta'^{1+\gamma}} d\eta' \\ & - \frac{\gamma}{2} \eta^{-\gamma} \int_{u_0 + \chi_0}^{\eta} \frac{f(\eta' - \chi_0)}{\eta'^{1-\gamma}} d\eta'. \end{aligned} \quad (5.13)$$

This expression is valid in the interval  $u_0 + \chi_0 < \eta < u_0 + 3\chi_0$  only.

#### D. Matching: Second epoch

We continue our integration of Eq. (5.1) and carry out the matching of Eqs. (5.5) and (5.6) in the interval  $u_0 + 3\chi_0 < \eta < u_0 + 5\chi_0$ . During this *second epoch*, the following events take place: (i) the new outgoing wave  $f_{\text{new}}(u)$  arrives at  $\chi = \chi_0$  and is partially transmitted and reflected; (ii) the reflected wave moves back toward  $\chi = 0$  and is totally reflected there; (iii) the new outgoing wave starts to move toward  $\chi = \chi_0$ .

During the second epoch,

$$\psi_{\text{left}} = f_{\text{new}}(u) + g_{\text{new}}(v), \quad (5.14)$$

where

$$\begin{aligned} f_{\text{new}}(u) = & -\frac{\gamma}{2} (u - \chi_0)^\gamma \int_{u_0 + 2\chi_0}^u \frac{f(u' - 2\chi_0)}{(u' - \chi_0)^{1+\gamma}} du' \\ & + \frac{\gamma}{2} (u - \chi_0)^{-\gamma} \int_{u_0 + 2\chi_0}^u \frac{f(u' - 2\chi_0)}{(u' - \chi_0)^{1-\gamma}} du' \end{aligned} \quad (5.15)$$

represents the new outgoing wave, and  $g_{\text{new}}(v)$  its partial reflection off the boundary. On the other hand,

$$\psi_{\text{right}} = \dot{F}(u) - \frac{1}{\eta} F(u) \quad (5.16)$$

represents the partially transmitted wave; because  $F(u)$  is continuous at  $u = u_0 + 2\chi_0$ , there is no need to distinguish the second-epoch  $F(u)$  with a label “new”.

The functions  $F(u)$  and  $g_{\text{new}}(v)$  are determined by Eqs. (5.9) and (5.10), in which we replace  $f(u)$  by  $f_{\text{new}}(u)$  and  $g(v)$  by  $g_{\text{new}}(v)$ . Equation (5.9) is solved under the conditions that  $F(u_0 + 2\chi_0)$  and  $\dot{F}(u_0 + 2\chi_0)$  match the values obtained from Eq. (5.11). This gives

$$\begin{aligned} F(u) = & \frac{1}{2} (u + \chi_0)^{1+\gamma} \left[ \int_{u_0}^{u_0 + 2\chi_0} \frac{f(u')}{(u' + \chi_0)^{1+\gamma}} du' \right. \\ & \left. + \int_{u_0 + 2\chi_0}^u \frac{f_{\text{new}}(u')}{(u' + \chi_0)^{1+\gamma}} du' \right] \end{aligned}$$

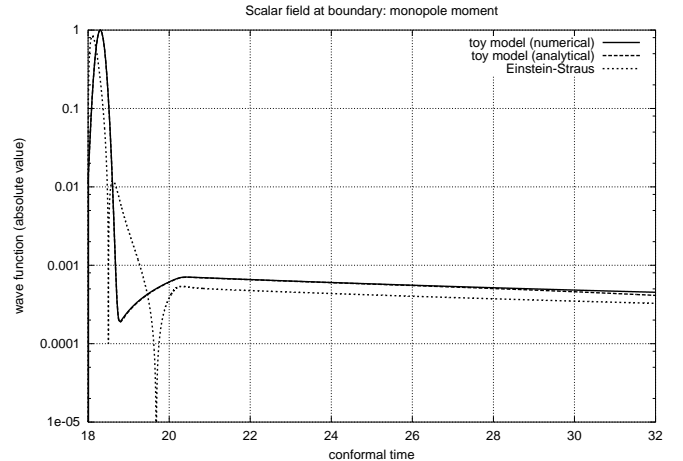


FIG. 14. A plot of the absolute value of the wave function on the boundary, as a function of conformal time  $\eta$ . The solid curve is obtained from a numerical integration of Eq. (5.1), starting with the gaussian wave packet described by Eq. (4.2). For this integration we set  $u_0 = 17$ ,  $v_0 = 17$ ,  $v_c = 17.3$ ,  $\sigma = 0.1$ , and  $\chi_0 = 1$ . The dashed curve is obtained from the analytical results of Eqs. (5.13) and (5.18), in which we substitute the totally reflected gaussian wave packet for  $f(u)$ . The two curves labelled “toy model” start to diverge at the end of the second epoch, when  $\eta = u_0 + 5\chi_0 = 22$ . The dotted curve represents a monopole wave in the Einstein-Strauss spacetime, which displays a similar late-time behavior.

$$\begin{aligned} & + \frac{1}{2} (u + \chi_0)^{1-\gamma} \left[ \int_{u_0}^{u_0 + 2\chi_0} \frac{f(u')}{(u' + \chi_0)^{1-\gamma}} du' \right. \\ & \left. + \int_{u_0 + 2\chi_0}^u \frac{f_{\text{new}}(u')}{(u' + \chi_0)^{1-\gamma}} du' \right], \end{aligned} \quad (5.17)$$

and  $g_{\text{new}}(v)$  can be obtained immediately from Eq. (5.10); because this result is not needed for further calculations, we shall not display it here. Substituting Eq. (5.17) into Eq. (5.16) and evaluating on the boundary, we obtain

$$\begin{aligned} \psi(\eta, \chi_0) = & f_{\text{new}}(\eta - \chi_0) + \frac{\gamma}{2} \eta^\gamma \left[ \int_{u_0 + \chi_0}^{u_0 + 3\chi_0} \frac{f(\eta' - \chi_0)}{\eta'^{1+\gamma}} d\eta' \right. \\ & \left. + \int_{u_0 + 3\chi_0}^{\eta} \frac{f_{\text{new}}(\eta' - \chi_0)}{\eta'^{1+\gamma}} d\eta' \right] \\ & - \frac{\gamma}{2} \eta^{-\gamma} \left[ \int_{u_0 + \chi_0}^{u_0 + 3\chi_0} \frac{f(\eta' - \chi_0)}{\eta'^{1-\gamma}} d\eta' \right. \\ & \left. + \int_{u_0 + 3\chi_0}^{\eta} \frac{f_{\text{new}}(\eta' - \chi_0)}{\eta'^{1-\gamma}} d\eta' \right]. \end{aligned} \quad (5.18)$$

This expression is valid in the interval  $u_0 + 3\chi_0 < \eta < u_0 + 5\chi_0$  only.

### E. Wave propagation in the toy model

Equation (5.13) gives  $\psi(\eta, \chi_0)$  in the interval  $u_0 + \chi_0 < \eta < u_0 + 3\chi_0$ , and Eq. (5.18) does the same in the interval  $u_0 + 3\chi_0 < \eta < u_0 + 5\chi_0$ . It can be checked that these values are continuous at  $\eta = u_0 + 3\chi_0$ . While integration of Eq. (5.1) could easily be carried out beyond the second epoch by repeated application of the general method, we shall stop here: to continue beyond this point would give rise to messy expressions that would not teach us anything new. The message of Eqs. (5.13) and (5.18) is already clear: The multiple transmissions and reflections that take place at  $\chi = \chi_0$  produce a wave function with a fairly complicated mathematical description, and its late-time behavior is not well described by a simple inverse power-law.

In Fig. 14 we compare the wave function obtained by integrating Eq. (5.1) to a  $l = 0$  wave in the Einstein-Straus spacetime. The figure reveals that both waves have a similar late-time behavior, providing support for our claim that wave propagation in the Einstein-Straus spacetime is governed mostly by partial transmissions and reflections.

### ACKNOWLEDGMENTS

This work was supported by the Natural Sciences and Engineering Research Council of Canada.

---

[1] R.H. Price, Phys. Rev. D **5**, 2419 (1972); **5**, 2439 (1972).  
 [2] E.W. Leaver, Phys. Rev. D **34**, 384 (1986).

[3] E.S.C. Ching, P.T. Leung, W.M. Suen, and K. Young, Phys. Rev. Lett. **74**, 2414 (1995); Phys. Rev. D **52**, 2118 (1995).  
 [4] N. Andersson, Phys. Rev. D **55**, 468 (1997).  
 [5] L. Barack, Phys. Rev. D **59**, 044016 (1999); 044017 (1999).  
 [6] S. Hod, gr-qc/0008001.  
 [7] S. Hod, Phys. Rev. D **58**, 104022 (1998); **61**, 024033 (2000); **61**, 064018 (2000).  
 [8] L. Barack and A. Ori, Phys. Rev. Lett. **82**, 4388 (1999); Phys. Rev. D **60**, 124005 (1999).  
 [9] L. Barack, Phys. Rev. D **61**, 024026 (2000).  
 [10] V. de la Cruz, J.E. Chase, and W. Israel, Phys. Rev. Lett. **24**, 423 (1970).  
 [11] C. Gundlach, R.H. Price, and J. Pullin, Phys. Rev. D **49**, 883 (1994); **49**, 890 (1994).  
 [12] W. Krivan, P. Laguna, and P. Papadopoulos, Phys. Rev. D **54**, 4728 (1996).  
 [13] W. Krivan, P. Laguna, P. Papadopoulos, and N. Andersson, Phys. Rev. D **56**, 3395 (1997).  
 [14] W. Krivan, Phys. Rev. D **60**, 101501 (1999).  
 [15] K. Glampedakis and N. Andersson, gr-qc/0102100; gr-qc/0103054  
 [16] P.R. Brady, C.M. Chambers, W. Krivan, and P. Laguna, Phys. Rev. D **55**, 7538 (1997).  
 [17] P.R. Brady, C.M. Chambers, W.G. Laarakkers, and E. Poisson, Phys. Rev. D **60**, 064003 (1999).  
 [18] J.S.F. Chan and R.B. Mann, Phys. Rev. D **55**, 7546 (1997); **59**, 064025 (1999).  
 [19] G.T. Horowitz and V.E. Hubeny, Phys. Rev. D **62**, 024027 (2000).  
 [20] B. Wang, C. Lin, and E. Abdalla, Phys. Rev. B **481**, 79 (2000).  
 [21] B. Wang, C.M. Mendes, and E. Abdalla, Phys. Rev. D **63**, 084001 (2001).  
 [22] A. Einstein and E.G. Straus, Rev. Mod. Phys. **17**, 120 (1945).  
 [23] W. Israel, Nuovo Cimento **44B**, 1 (1966); **48B**, 463 (1967).  
 [24] For example, C.M. Bender and S.A. Orszag, *Advanced Mathematical Methods for Scientists and Engineers* (McGraw-Hill, New York, 1978), Sec. 1.5.